Analytical Model for Drag Reduction on Liquid-Infused Structured Non-Wetting Surfaces

SCHOLARONE™
Manuscripts

Analytical Model for Drag Reduction on Liquid-Infused Structured Non-Wetting Surfaces

S. Hatte and R. Pitchumani[*]

Advanced Materials and Technologies Laboratory
Department of Mechanical Engineering
Virginia Tech
Blacksburg, Virginia 24061-0238, United States

ABSTRACT

Liquid-infused structured non-wetting surfaces provide alternating no-slip and partial slip boundary conditions to the fluid flow, resulting in reduced friction at the interface. In this paper, an analytical model is developed for the evaluation of effective slip and, in turn, friction factor and drag reduction on liquid-infused structured non-wetting surfaces. By considering the entire range of anisotropy and heterogeneity of the surface structures as well as the full range of partial slip offered by the infusion liquid, the present model overcomes eliminates empirical fitting or correlations that are inherent in previous studies. Based on the effective slip length, drag reduction and skin friction coefficient values for Newtonian flow between two infinite parallel plates and flow in round tubes are presented. Extension of Moody charts for non-wetting surfaces and design maps of surface meso/micro/nano texturing for achieving desired drag reduction are presented for a broad range of engineering applications. The article further presents independent validation of the model across experimental and computational data from the literature and brings together several previous studies in a unified manner.

KEYWORDS

---

[*] Author for correspondence: pitchu@vt.edu

1. INTRODUCTION

In the past few decades, structured non-wetting surfaces have received significant interest for their role in a multitude of applications such as drag reduction [1–3], phase change heat transfer [4–6], self-cleaning surfaces [7–9], anti-icing surfaces [10–12], etc. Structured non-wetting surfaces are known to offer high static contact angle, low contact angle hysteresis, and a finite amount of slip under dynamic fluid flow conditions. The characteristic parameters that give rise to the aforementioned properties of non-wetting surfaces are the bare surface hydrophobicity, micro/nano-scale roughness features, and the presence of infusion liquid in the valleys of the roughness features.

Structured non-wetting surfaces are broadly categorized into two types: (1) slippery liquid-infused porous surfaces and (2) superhydrophobic surfaces. Slippery liquid-infused porous surfaces (SLIPS) are created by impregnating a liquid in the voids created by the porous micro/nano-scale structures, as depicted in Figure 1a. The choice of infusion liquid is governed by its expected physical properties such as immiscibility with the working fluid, high affinity towards the base surface [13,14], high thermal conductivity, low surface tension and low viscosity. On the other hand, superhydrophobic (SH) surfaces have air trapped in the cavities created by micro/nano-structures[15]. Note that the limiting case of an infinite slip length (shear-free) on infusion liquid corresponds to the presence of air pockets in the asperity valleys, and the structured liquid infused non-wetting surfaces default to conventional SH surfaces. Therefore, in the present work, the term *structured liquid infused non-wetting surfaces* is used generically to represent both SLIPS and SH surfaces.

Typical static contact angle measurements on SLIPS (SH) surfaces are 120–140° (> 150°) and the corresponding range of contact angle hysteresis is 5–10° (< 4°). Under dynamic conditions, fluid flow over a typical liquid-infused structured non-wetting surface experiences alternating (periodic) partial slip and no-slip boundary conditions at the interface.[16,17] The partial slip condition offered by the infused liquid gives rise to a significant reduction in the friction compared to the case of smooth solid surfaces that offer a no-slip boundary condition throughout. As a result, the extent of effective slip length correlates directly to the drag reduction on liquid-infused structured non-wetting surfaces.

Estimating the effective slip of fluid flow over structured non-wetting surfaces has been explored in the literature via numerical simulations, experiments, or statistical correlations. Rothstein[18] and Voronov et al.[19] have systematically summarized seminal studies on effective slip length and drag reduction on structured non-wetting surfaces. In contrast, there are relatively scant closed-form analytical models that can predict the effective slip length based on surface topographical information. Further, most of the existing studies are limited to structured SH surfaces whereas liquid infused structured surfaces are relatively less explored in the literature. Philip[20] developed analytical models for SH longitudinal- and transverse-striped geometry on flat and curved surfaces (round tubes). Further, Lauga and Stone[21] expanded the analysis with asymptotic behavior of slip lengths on longitudinal and transverse striped geometries. However, their analysis was restricted and is valid to striped geometries only. In addition, Feuillebois et al.[22,23] presented bounds through minimum and maximum possible effective slip lengths on striped geometry and synthetic fractal pattern of nested circles. In Feuillebois et al.[24] a theoretical model is presented for the optimization of transverse flow over a two-component structured surface. However, the exact nature of the effective slip length relationship with the area fractions of solid and non-solid regions is not covered in their study. Belyaev and Vinogradova[25] incorporated the contribution of finite slip at the infused liquid for transverse- and longitudinal-striped geometries. Davis and Lauga[26] developed an asymptotic analytical model in the vanishing region of solid area fraction on SH surfaces with square posts geometry. Ybert et al.[27] presented scaling laws for a SH square posts geometry, although their analysis is limited to the vanishing regions of solid and non-solid area fractions, does not incorporate the contribution of finite slip offered by infused liquid region, and does not consider inhomogeneity of the structures (e.g. rectangular posts). Solomon et al.[28] presented a model for drag reduction (equivalently, effective slip length) on liquid infused structured non-wetting surfaces. However, the underlying assumption of a linear velocity profile in the infused liquid layer limits the applicability of their model to highly viscous infusion liquids. Cottin-Bizonne et al.[29] developed a scaling law for slippage on superhydrophobic fractal surfaces, which does not directly apply to structured non-wetting surfaces. A number of experimental studies[30–32] have reported significant effective slip

(and drag reduction) on structured non-wetting surfaces, but do not establish a direct correlation between the measured slip length and surface topology.

It is evident from the foregoing discussion that the existing studies have mostly focused on the effective slip length and the drag characteristics of striped surface textures or other synthetic, isotropic homogeneously patterned surfaces. A general analytical treatment of non-wetting surface textures with anisotropy and heterogeneity and infused with any fluid medium is presently lacking. Such a treatment is of much interest as the field and applications of liquid infused and textured non-wetting surfaces continues to grow. Furthermore, it is of interest to determine the conditions under which such surfaces indeed offer a drag reduction advantage, and to tailor the design of the textures for a desired drag reduction performance, which are also lacking in the currently available studies.

With the above motivation, in the present study, an analytical expression is developed for calculating the effective slip length on a generic fluid-infused structured non-wetting surfaces. The present formulation overcomes a number of limitations observed in the models previously reported in the literature by accounting for the finite slip offered by the non-solid regions of the surface, and the heterogeneity and anisotropy of structures. The analytical model presents a unified treatment of the different topographies and reduces to the striped geometry that's often considered in the literature under limiting cases of the geometric parameters. Based on the effective slip length calculations from the analytical model, drag reduction and skin friction coefficient values for Newtonian flow between two infinite parallel plates (Figure 2a) and flow in round tubes (Figure 2b) are quantified. The friction coefficient expression provides, for the first time, an extension of the conventional Moody diagram to flow in channels and cylindrical geometries with non-wetting surfaces. The predictions of effective slip length and drag reduction from the present study are shown to be in good agreement with experimental and computational data obtained from the literature. Further, design maps are presented for tailoring the surface textures for achieving desired drag reduction in applications. Overall, the model is shown to be generally applicable to a wide range of topographies, infused liquid parameters, and channel thickness, which forms the primary contribution of the article.

The paper is organized as follows: first, a geometric description of the structured non-wetting surface is provided in section 2, followed by a mathematical description of effective slip length, drag reduction and friction coefficient calculations in section 3. Next, the effects of surface structural parameters and flow conditions, followed by validation of the present model with the data obtained from the literature is presented in section 4.

2. GEOMETRICAL DESCRIPTION

Figure 1a shows an isometric view of a liquid-infused anisotropic heterogeneously patterned structured (AHePS) surface. The coordinate system for the analysis is established with the x-axis being along the fluid flow direction, y-axis being perpendicular to the flow direction in the plane of the surface and the z-axis being perpendicular to the plane of the surface and the flow direction. The periodic length scales of the post structures, as shown in Figure 1a in the x- and y- directions, are L_x and L_y, respectively, such that for an isotropic structured surface, $L_x = L_y = L$. Fluid flow over such a surface experiences alternating boundary conditions at the interface of flowing fluid and solid/infused liquid regions. In the present study, surface heterogeneity is defined by the inequality of the length scales of the infused liquid regions, δ_x and δ_y. Accordingly, homogeneous and heterogeneous structures refer to square post $(\delta_x = \delta_y)$ and rectangular post $(\delta_x \neq \delta_y)$ geometries, respectively.

3. MATHEMATICAL DESCRIPTION

A pressure-driven laminar fluid flow between two infinite parallel plates separated by a distance H (Figure 2a) is considered for the effective slip length calculation, although the expressions for the slip length are generally applicable to flow in a cylindrical tube of radius R (Figure 2b) with the same structured surface topography. The surfaces of the top and bottom plates in contact with the flowing fluid are considered to be liquid-infused structured non-wetting surfaces, as illustrated in Figure 2a. The analytical modeling of the effective slip length for flow over a typical liquid-infused structured non-wetting surface (Figure 1a) is developed by considering generalized partial slip boundary conditions over both the solid $(b_s \geq 0)$ and the infused liquid regions $(b_f \geq 0)$ for the calculations of effective slip length on longitudinal- and

transverse-striped geometries, as shown schematically in Figures 1b and 1d, respectively. The present work generalizes their analysis with generalized slip boundary conditions, $b_s \geq 0$ and, at the respective solid and infused liquid interfaces. With these generalized expressions for the effective slip lengths for transverse- and longitudinal-striped surfaces as basis, a further contribution of the modeling is the determination of the effective slip lengths of surfaces textured with periodic rectangular post geometries, for application to a wide class of non-wetting superhydrophobic or slippery liquid infused surfaces. Based on the effective slip length, expressions for drag reduction and friction factor are presented for fluid flow in rectangular and cylindrical tube geometries.

3.1 Effective Slip Length of Longitudinal- and Transverse-striped Liquid Infused Surfaces

For a fully developed pressure-driven laminar Poiseuille flow between two infinite parallel plates (separated by distance H, Figure 2a) structured with longitudinal stripes (Figure 1b), the governing conservation of momentum may be written as per eq. 1a in Table 1, where u and $\frac{dp}{dx}$ are the velocity component and pressure gradient in the flow direction, respectively. The associated boundary conditions (eqs. 1b–e) are expressed in Table 1. For the case of longitudinal-striped geometry (Figure 1b), the symmetry of velocity profile about $y = 0$ and periodicity of L_y along the y-axis lead to eqs. 1b and 1c, respectively, as shown in Table 1. Symmetry of fluid flow velocity profile about the center of the channel $\left(z = \frac{H}{2}\right)$ leads to eq. 1d (Table 1). The boundary conditions at the bottom structured wall, $z = 0$, take the general form as per eq. 1e in Table 1, where $b(y)$ is the *local* slip length for fluid flow over an interface with alternating partial slip boundary conditions over the solid and the liquid infused regions.

For a longitudinal-striped geometry, the governing equation (eq. 1a) and the associated boundary conditions (eq. 1b-e) are solved using the method of perturbation[25] by considering the velocity to be $u(y,z) = u_0(z) + u'(y,z)$, where u_0 is the base parabolic velocity profile for a fully developed flow in a rectangular channel with a partial slip length of b_s at the fluid/solid interface, given by:

$$u_0(z) = \frac{1}{2\eta}\left(-\frac{dp}{dx}\right)\left(z^2 - \frac{H^2 z}{H + b_s} - \frac{H^2 b_s}{H + b_s}\right) \#(2)$$

Substituting $u(y,z) = u_0(z) + u'(y,z)$, with $u_0(z)$ given by eq. 2, in eqs. 1a–e in Table 1, results in a Laplace equation for $u'(y,z)$ (eq. 3a in Table 1) and associated conditions (eqs. 3b–e in Table 1), as follows. Since the base velocity $u_0(z)$ (eq. 2) is independent of y, it follows from eq. 1b that the perturbation velocity $u'(y,z)$ is symmetric about $y = 0$, expressed as eq. 3b in Table 1. The base velocity $u_0(z)$ at the bottom wall ($z = 0$) leads to the boundary condition in eq. 1c to periodicity of perturbation velocity, u', expressed as eq. 3c in Table 1. The symmetry of base velocity profile u_0 about $z = \frac{H}{2}$ (as per eq. 1d) leads to the symmetry of perturbation velocity profile u' about $z = \frac{H}{2}$ as expressed in eq. 3d in Table 1. The vanishing base velocity at the bottom wall ($z = 0$) leads to a composite boundary conditions in the infused liquid and solid regions as given by eq. 3e in Table 1 corresponding to the local slip lengths being b_f and b_s, respectively.

Using the method of separation of variables, eqs. 3a–e are solved to get the perturbation velocity, $u'(y,z)$ in the following form for relatively thicker channels with $\frac{L_y}{H} \leq 0.1$,

$$u'(y,z) = \frac{L_y^2}{4\pi^2\eta}\frac{dp}{dx}\left[\frac{\alpha_0}{2} + \sum_{n=1}^{\infty}\alpha_n \cos\left(\frac{2\pi n}{L_y}y\right)e^{-\frac{2\pi n}{L_y}z}\right] \#(4)$$

where α_0 and α_n are constant coefficients. From the total velocity $u(y,z) = u_0(z) + u'(y,z)$, comprising the base velocity profile $u_0(z)$ (eq. 2) and the perturbation velocity profile $u'(y,z)$ (eq. 4), the effective slip length for longitudinal stripes is obtained as,

$$\overline{b}_L = \frac{\int_{-\frac{L_y}{2}}^{\frac{L_y}{2}} u(y,0)dy}{\int_{-\frac{L_y}{2}}^{\frac{L_y}{2}} \frac{\partial u(y,0)}{\partial z}dy} = b_s + \frac{L_y}{\pi}\left(\frac{L_y\alpha_0}{4\pi H}\right) \#(5)$$

Eq. 5 suggests that the effective slip length is dependent only on the leading coefficient α_0 in the perturbation velocity profile (eq. 4) since the harmonic terms in eq. 4 average to zero. According to Sneddon[33], α_0 may be expressed as:

$$\alpha_0 = \sqrt{2}\int_0^{\frac{\pi\delta_y}{L_y}} h(t)dt \#(6)$$

where, for the present case of flow over a surface with slip lengths of b_s and b_f over the solid surface and the infused liquid regions, respectively, $h(t)$ is obtained as: $h(t) = \frac{2}{\pi} \frac{d}{dt}$

$\int_0^t \frac{\sin(\frac{\zeta}{2})}{\sqrt{\cos(\zeta) - \cos(t)}} \left[\left(1 - \frac{b_s}{b_f}\right) \cdot \frac{\pi H}{L_y} \zeta - \frac{\alpha_0 L_y}{4 b_f} \right] d\zeta$. Substituting for $h(t)$ in eq. 6 and, in turn, the resulting expression for α_0 into eq. 5, the generalized expression for the effective slip length for longitudinal-striped geometry is obtained in the following form:

$$\overline{b}_L = b_s + \frac{L_y}{\pi} \left(\frac{\left(1 - \frac{b_s}{b_f}\right) \cdot \ln\left[\sec\left(\frac{\pi}{2} \cdot \frac{\delta_y}{L_y}\right)\right]}{1 + \frac{L_y}{\pi b_f} \ln\left[\sec\left(\frac{\pi}{2} \cdot \frac{\delta_y}{L_y}\right) + \tan\left(\frac{\pi}{2} \cdot \frac{\delta_y}{L_y}\right)\right]} \right) \#(7)$$

The foregoing expression is valid for relatively thick channels $\left(\frac{L_y}{H} \leq 0.1\right)$ and for round tubes $\left(\frac{L_y}{R} \leq 0.1\right)$. As consistency checks, it is verified that as $\frac{\delta_y}{L_y} \to 0$, which denotes the case of vanishing infused liquid region, the expression in eq. 7 reduces to b_s, which is the effective slip length on a smooth surface offering uniform slip length of b_s throughout. Similarly, for $\frac{\delta_y}{L_y} \to 1$, which denotes the case of vanishing solid region, the expression correctly reduces to b_f.

For the case of transverse-striped geometry (Figure 1d and 1e), the dependence of pressure gradient on x leads to the consideration of a stream function $\psi(x,z)$ and vorticity $\vec{\omega}(x,z)$. The resultant two-dimensional velocity field in the x-z plane is represented in terms of the velocity components $u(x,z)$ and $w(x,z)$ in the x- and z- directions, respectively, such that $u(x,z) = \frac{\partial \psi}{\partial z}$, and w $(x,z) = -\frac{\partial \psi}{\partial x}$. Note that the definition of a stream function implicitly satisfies the continuity equation for incompressible flow, $\frac{\partial u}{\partial x} + \frac{\partial w}{\partial z} = 0$. The vorticity vector, $\vec{\omega}(x,z)$, has only one non-zero component, in the y-direction, given by $\omega(x,z) = \frac{\partial u}{\partial z} - \frac{\partial w}{\partial x}$. Substituting the expressions of velocity components in terms of stream function, $u(x,z) = \frac{\partial \psi}{\partial z}$ and $w(x,z) = -\frac{\partial \psi}{\partial x}$, into the expression of z-component of vorticity leads to governing equation as expressed by eq. 8a in Table 2. The second governing equation is a vorticity transport formulation as expressed by eq. 9a in Table 2, which is obtained by subtracting the x derivative of z- component of momentum conservation equation from the z derivative of x- component of momentum conservation equation.

The presence of impenetrable walls at $z = 0$ and $z = H$ leads to boundary conditions: $w(x,0) = 0$ and $w(x,H) = 0$, respectively, which are rewritten in terms of the stream function in eqs. 8b–c of Table 2. Equations 8b and 8c, both being Neumann boundary conditions, necessitates additional information for a unique solution of the stream function, $\psi(x,z)$. These additional conditions are obtained by defining a reference value for stream function at an arbitrary point $(x_0, y_0,0)$ in the plane $z = 0$ such that: $\psi(x_0,y_0,0) = 0$. The stream function at the top wall, ψ_H, is then equal to the volumetric flow rate between the top and the bottom walls, $\frac{H^3}{12\eta}\left(-\frac{dp}{dx}\right)$, as per the methodology given in Priezjev et $al.$[34], where $-\frac{dp}{dx}$ is a positive pressure gradient and η is the viscosity of the fluid flowing in the channel. Figures 1d-e show that the bottom wall $(z = 0)$ consists of an infinite number of symmetry planes located at the geometric centers of solid and infused liquid regions: $x = n\frac{L_x}{2}$, for all integer values of n. The same symmetry appears on the upper wall $(z = H)$ as well. As a result, the velocity component in the direction of flow satisfies $\frac{\partial u}{\partial x}(x = n\frac{L_x}{2},z) = 0$. From the continuity equation it, then, follows that $w(x,z)$ is invariant with respect to z at the symmetry plane locations and is given as: $\frac{\partial w}{\partial z}(x = n\frac{L_x}{2},z) = 0$. Combined with the impenetrable wall conditions, $w(x,z = 0) = w(x,z = H) = 0$, we obtain that $w(x = n\frac{L_x}{2},z) = 0$, which is rewritten in terms of stream function and expressed by eqs. 8d-e in Table 2, for one periodic segment of the transverse striped wall $0 \leq x \leq \frac{L_x}{2}$.

For a fully developed steady state flow, the symmetry of velocity component in the direction of flow given by $u(x,z) = u(-x,z)$ together with the continuity equation leads to symmetry of the z-component of velocity given by $w(x,z) = w(-x,z)$ with $w\left(x = n\frac{L_x}{2},z\right) = 0$ and $\frac{\partial^2 w}{\partial z^2}(x = n\frac{L_x}{2},z) = 0$. Substituting this into the expression for the x- derivative of vorticity component leads to boundary conditions as expressed by eqs. 9b-c. The Navier slip boundary conditions at the bottom structured wall, $z = 0$, and top structured wall, $z = H$, take the general forms as per eqs. 9d and 9e, respectively, in Table 2, where $b(x)$ is the $local$ slip length for fluid flow over an interface with alternating partial slip boundary conditions over the solid and the liquid infused regions.

For a transverse-striped geometry, the governing equations (eqs. 8a and 9a) and their respective associated boundary conditions (eqs. 8b–e, 9b–e) are solved using the methodology similar to the case of longitudinal striped geometry, by considering the stream function to be $\psi(x,z) = \psi_0(z) + \psi'(x,z)$ and vorticity to be $\omega(x,z) = \omega_0(z) + \omega'(x,z)$, where ψ_0 and ω_0 are the base stream function and vorticity profiles for a fully developed flow in a rectangular channel with partial slip length of b_s at the bounding surfaces of the channel, given by:

$$\psi_0(z) = -\frac{1}{2\eta}\frac{dp}{dx}z\left(\frac{z^2}{3} - \frac{zH}{2} - b_sH\right) \#(10)$$

$$\omega_0(z) = -\frac{1}{\eta}\frac{dp}{dx}\left(z - \frac{H}{2}\right)\#(11)$$

The perturbation stream function, $\psi'(x,z)$, and perturbation vorticity function, $\omega'(x,z)$, are determined by substituting $\psi(x,z) = \psi_0(z) + \psi'(x,z)$ and $\omega(x,z) = \omega_0(z) + \omega'(x,z)$ with $\psi_0(z)$ and $\omega_0(z)$ given by eqs. 10 and 11, respectively, in eqs. 8a and 9a, and solving the resulting governing equations (eqs. 12a, 13a in Table 2) along with their respective associated boundary conditions (eqs. 12b–e, 13b–e in Table 2) to obtain:

$$\psi'(x,z) = \frac{HL_x^2}{4\pi^2\eta}\frac{dp}{dx}\left[\beta_0\frac{z}{H}\left(1 - \frac{1}{4}\frac{z}{H}\right) + \sum_{n=1}^{\infty}\left(\beta_n \cdot \frac{L_x}{4\pi n}z\right)\cos\left(\frac{2\pi n}{L_x}x\right)e^{-\frac{2\pi n}{L_x}z}\right]\#(14)$$

and

$$\omega'(x,z) = \frac{L_x^2}{4\pi^2\eta H}\frac{dp}{dx}\left[-\frac{\beta_0}{2} + \sum_{n=1}^{\infty}\beta_n \cdot \cos\left(\frac{2\pi n}{L_x}x\right)e^{-\frac{2\pi n}{L_x}z}\right]\#(15)$$

As in the case of longitudinal striped geometry, the foregoing expressions are valid for $\frac{L_y}{H} \leq 0.1$. With the base stream function $\psi_0(z)$ (eq. 10) and perturbation stream function $\psi'(x,z)$ (eq. 14), the velocity can be determined as $u(x,z) = \left(\frac{\partial\psi_0}{\partial z} + \frac{\partial\psi'}{\partial z}\right)$ and the effective slip length for transverse-striped geometry, $\bar{b}_T$, can be obtained as:

$$\bar{b}_T = \frac{\int_{-\frac{L_x}{2}}^{\frac{L_x}{2}} u(x,0)dx}{\int_{-\frac{L_x}{2}}^{\frac{L_x}{2}} \frac{\partial u(x,0)}{\partial z}dx} = b_s + \frac{L_x}{2\pi}\left(\frac{L_x\beta_0}{\pi H}\right)\#(16)$$

Note that, similar to eq. 5, eq. 16 suggests that the effective slip length is dependent only on the leading coefficient β_0 in the perturbation stream function (eq. 14). According to Sneddon[33], β_0 may be expressed as $\beta_0 = \sqrt{2} \int_0^{\frac{\pi \delta_x}{L_x}} g(t) dt$ where, for the present case of flow over a surface with slip lengths of b_s and b_f over the solid surface and the infused liquid regions, respectively, $g(t)$ is obtained as: $g(t) = \frac{2}{\pi} \frac{d}{dt} \int_0^t \frac{\sin\left(\frac{\zeta}{2}\right)}{\sqrt{\cos(\zeta) - \cos(t)}} \left[\left(1 - \frac{b_s}{b_f}\right) \cdot \frac{\pi H}{L_x} \zeta - \frac{\beta_0 L_x}{8 b_f} \right] d\zeta$. Following the approach similar to the case of longitudinal stripes, substituting the expression of $g(t)$ into the integral expression of β_0 leads to an effective slip length formulation for transverse stripes from eq. 16 expressed in the following form for a general case of partial slip at the fluid-solid and the fluid-infused liquid interfaces:

$$\bar{b}_T = b_s + \frac{L_x}{2\pi} \left(\frac{\left(1 - \frac{b_s}{b_f}\right) \ln\left[\sec\left(\frac{\pi}{2} \cdot \frac{\delta_x}{L_x}\right)\right]}{1 + \frac{L_x}{2\pi b_f} \ln\left[\sec\left(\frac{\pi}{2} \cdot \frac{\delta_x}{L_x}\right) + \tan\left(\frac{\pi}{2} \cdot \frac{\delta_x}{L_x}\right)\right]} \right) \#(17)$$

Similar to the expression for longitudinal stripes with non-zero slip in the solid region $(\bar{b}_L)$, eq. 17 satisfies all the physical consistency checks.

3.2 Effective Slip Length of Anisotropic Heterogeneously Patterned Surfaces

The effective slip length of a liquid infused anisotropic heterogeneously patterned surface (AHePS), as depicted in Figure 1a, is obtained by considering a no-slip boundary condition over the solid regions $(b_s = 0)$, for which eqs. 7 and 17 reduce to:

$$\bar{b}_L^0 = \frac{L_y}{\pi} \left(\frac{\ln\left[\sec\left(\frac{\pi}{2} \cdot \frac{\delta_y}{L_y}\right)\right]}{1 + \frac{L_y}{\pi b_f} \ln\left[\sec\left(\frac{\pi}{2} \cdot \frac{\delta_y}{L_y}\right) + \tan\left(\frac{\pi}{2} \cdot \frac{\delta_y}{L_y}\right)\right]} \right) \#(18)$$

$$\overline{b}_T^0 = \frac{L_x}{2\pi}\left(\frac{\ln\left[\sec\left(\frac{\pi}{2}\cdot\frac{\delta_x}{L_x}\right)\right]}{1+\frac{L_x}{2\pi b_f}\ln\left[\sec\left(\frac{\pi}{2}\cdot\frac{\delta_x}{L_x}\right)+\tan\left(\frac{\pi}{2}\cdot\frac{\delta_x}{L_x}\right)\right]}\right)\#(19)$$

where the superscript 0 denotes the case of no slip at the solid-liquid interface. A liquid infused AHePS surface with a regular array of rectangular post geometries can be considered as a superposition of transverse- and longitudinal-striped geometries. Fluid flow over such a surface experiences alternating no-slip and finite slip boundary conditions in x- and y- directions (Figure 1a) at the interface. Considering rows of posts along the flow direction, as marked by the dashed boxes, T, in Figure 3a, the fluid flow over each such region experiences alternating boundary conditions in the direction of flow that is equivalent to the flow past a transverse-striped geometry. Therefore, the effective slip length for flow over each such row is given by eq. 19.

The AHePS geometry may now be considered as longitudinal stripes of the dashed regions, T, in Figure 3a, each with an effective slip length, $\overline{b}_T^0$, given by eq. 19, alternating with liquid infused regions of slip length, b_f. Referring to the case of longitudinal-striped geometry with finite slip lengths of $b_s = \overline{b}_T^0$ and b_f, as derived in eq. 7, the effective slip length for a liquid-infused AHePS surface, $\overline{b}$, may be expressed in terms of $\overline{b}_T^0$ and $\overline{b}_L^0$ and b_f as:

$$\overline{b} = \overline{b}_T^0 + \overline{b}_L^0 - \frac{\overline{b}_T^0 \cdot \overline{b}_L^0}{b_f}\#(20)$$

The expression for the effective slip length $(\overline{b})$ is symmetric in terms of the contributing individual effective slip lengths of the longitudinal- $(\overline{b}_L^0)$ and transverse- $(\overline{b}_T^0)$ striped geometries. The same analytical relationship as presented in eq. 20 is obtained if the longitudinal stripes are considered first (as depicted in Figure 3b) followed by the equivalent transverse stripes.

The analytical solution (eq. 20) for effective slip length on a liquid infused AHePS surface takes into consideration the anisotropy of the structural pattern $(L_x \neq L_y)$, heterogeneity of the structures $(\delta_x \neq \delta_y)$, and the contribution of the finite slip (b_f) offered by the infusion liquid. From this general treatment of patterned surfaces, specific expressions may be derived for the effective slip length of an *isotropic heterogeneously* patterned structured (IHePS) surface by setting the periodic length scales to be equal, i.e., $L_x = L_y = L$, in eqs. 18–20. In this case, since $\delta_x \neq \delta_y$, the

solid structures take the shape of rectangular posts. For a liquid-infused *isotropic homogeneously patterned structured* (IHoPS) surface with a regular square post geometry, $\delta_x = \delta_y = \delta$, and it is convenient to introduce a solid area fraction of the surface, $\varphi_s = \left(1 - \frac{\delta}{L}\right)^2$, such that $\frac{\delta_x}{L_x} = \frac{\delta_y}{L_y} = \frac{\delta}{L} = (1 - \sqrt{\varphi_s})$. Introducing the dimensionless structural parameters, $\frac{\delta_x}{L_x}$ and $\frac{\delta_y}{L_y}$ in eqs. 18 and 19, the effective slip lengths, $\bar{b}_L^0$ and $\bar{b}_T^0$ are then expressed in terms of the solid fraction, φ_s, as:

$$\bar{b}_L^0 = \frac{L}{\pi}\left(\frac{\ln\left[\sec\left(\frac{\pi}{2}(1 - \sqrt{\varphi_s})\right)\right]}{1 + \frac{L}{\pi b_f}\ln\left[\sec\left(\frac{\pi}{2}(1 - \sqrt{\varphi_s})\right) + \tan\left(\frac{\pi}{2}(1 - \sqrt{\varphi_s})\right)\right]}\right) \tag{21}$$

$$\bar{b}_T^0 = \frac{L}{2\pi}\left(\frac{\ln\left[\sec\left(\frac{\pi}{2}(1 - \sqrt{\varphi_s})\right)\right]}{1 + \frac{L}{2\pi b_f}\ln\left[\sec\left(\frac{\pi}{2}(1 - \sqrt{\varphi_s})\right) + \tan\left(\frac{\pi}{2}(1 - \sqrt{\varphi_s})\right)\right]}\right) \tag{22}$$

using which, the effective slip length for the IHoPS $\bar{b}$ is obtained from eq. 21 in terms of φ_s and $\frac{L}{b_f}$.

3.3 Drag Reduction and Friction Coefficient on Liquid Infused Patterned Surfaces

With the effective slip length over structured non-wetting surfaces given by eq. 21, the engineering parameters that govern fluid flow namely, drag reduction and friction coefficient, are quantified by considering two cases corresponding to the two flow geometries in Figure 2:

3.3.1 Fluid flow between two parallel infinite plates separated by a distance H:

Considering a pressure driven laminar flow between two parallel infinite plates (separated by distance H) with no-slip boundary conditions at the walls, the total volume flow rate is given by: $Q_0 = -\frac{H^3}{2\eta}\left(\frac{\partial p}{\partial x}\right)_0\left(\frac{1}{6}\right)$. Similarly, the volumetric flow rate for the same flow configuration with liquid infused AHePS surfaces with an effective slip length of $\bar{b}$, given by eq. 21, is calculated as: $Q_s = -\frac{H^3}{2\eta}\left(\frac{\partial p}{\partial x}\right)_s\left(\frac{1}{6} + \frac{\bar{b}}{H}\right)$. In the expressions for the volumetric flow rate, subscripts 0 and s denote the cases of geometries with smooth (no-slip boundary condition throughout) and structured

non-wetting surfaces (with an effective finite slip). Also, the negative sign offsets the negative value of $\frac{\partial p}{\partial x}$ resulting in positive flow rate values. A drag reduction, D_R, is defined as the relative difference between the pressure gradients for AHePS and smooth surfaces, for the same volumetric flow rate ($Q_0 = Q_s$), such that

$$D_{R,H} = \frac{\left(\frac{\partial p}{\partial x}\right)_0 - \left(\frac{\partial p}{\partial x}\right)_s}{\left(\frac{\partial p}{\partial x}\right)_0} = \frac{6\bar{b}}{H + 6\bar{b}} \tag{23}$$

where $\bar{b}$ for AHePS and IHePS ($L_x = L_y = L$) are given by eqs. 18–20, and for IHoPS by eqs. 20–22.

Drag reduction is a relative parameter that compares the case of structured non-wetting surface to the conventional smooth surface. An intrinsic measure of reduced friction on structured non-wetting surfaces may be quantified in terms of skin friction coefficient. For a pressure-driven laminar flow between two infinite parallel plates with AHePS surfaces separated by distance H, the average velocity across the cross-sectional area is given by: $\bar{u}_s = -\frac{H^2}{2\eta}\left(\frac{\partial p}{\partial x}\right)_s \left(\frac{1}{6} + \frac{\bar{b}}{H}\right)$ and the wall shear stress at $z = 0$ may be expressed as: $\tau_s = \eta\frac{\partial u}{\partial z} = \bar{u}_s \cdot \frac{6\eta}{6\bar{b} + H}$, where η is the fluid viscosity. The skin friction coefficient defined as, $C_{f,H} = \frac{|\tau_s|}{\frac{1}{2}\rho\bar{u}_s{}^2}$, where ρ is the fluid density, is then derived as:

$$C_{f,H} = \frac{|\tau_s|}{\frac{1}{2}\rho\bar{u}_s{}^2} = \frac{12H}{(6\bar{b} + H)} \cdot \frac{1}{Re_H} \tag{24}$$

where $\bar{b}$ for AHePS and IHePS ($L_x = L_y = L$) are given by eqs. 18–20, and for IHoPS by eqs. 20–22. Further, Re_H is the Reynolds number defined based on the channel height, H, as the characteristic dimension: $Re_H = \frac{\rho\bar{u}_s H}{\eta}$.

3.3.2 Fluid flow in a round pipe (cylindrical geometry):

For pressure-driven laminar flow through a round pipe of radius R (Figure 2b), the volumetric flow rate with no surface texturing is given by, $Q_0 = -\frac{\pi R^4}{\eta}\left(\frac{\partial p}{\partial x}\right)_0 \cdot \left(\frac{1}{8}\right)$, and with an AHePS surface on the inside of the pipe is expressed as $Q_s = -\frac{\pi R^4}{\eta}\left(\frac{\partial p}{\partial x}\right)_s \cdot \left(\frac{1}{8} + \frac{\bar{b}}{2R}\right)$. Defining a drag reduction, D_R,

as in eq. 23, the drag reduction for fluid flow through a round pipe with AHePS surface is obtained as follows:

$$D_{R,R} = \frac{\left(\frac{\partial p}{\partial x}\right)_0 - \left(\frac{\partial p}{\partial x}\right)_s}{\left(\frac{\partial p}{\partial x}\right)_0} = \frac{4\bar{b}}{R + 4\bar{b}} \tag{25}$$

A skin friction coefficient may be derived following the same approach as that for flow in a rectangular channel discussed above. For a pressure-driven flow through a round pipe of radius, R, with an AHePS surface, the average flow velocity, $\bar{u}_s = -\frac{R^2}{\eta}\left(\frac{\partial p}{\partial x}\right)_s\left(\frac{1}{8} + \frac{\bar{b}}{2R}\right)$, and wall shear stress at $r = R$, $\tau_s = \bar{u}_s \cdot \frac{4\eta}{4\bar{b} + R}$, lead to the friction coefficient as:

$$C_{f,R} = \frac{|\tau_s|}{\frac{1}{2}\rho\bar{u}_s^2} = \frac{16R}{(4\bar{b} + R)} \cdot \frac{1}{Re_D} \tag{26}$$

It is evident from eq. 23 and 25 that for a pressure-driven flow under laminar conditions, the expressions of drag reduction are solely a function of the geometric parameters of the patterned surface and are independent of fluid flow conditions such as the Reynolds number, whereas the skin friction coefficient, eq. 24 and 26, is a function of both the geometric parameters and the Reynolds number based on the respective characteristic length.

4. RESULTS AND DISCUSSION

Figure 4 shows the variation of dimensionless effective slip length of liquid infused longitudinal- $\left(\frac{\bar{b}_L^0}{L_y}\right)$ and transverse-striped $\left(\frac{\bar{b}_T^0}{L_x}\right)$ geometries assuming no-slip boundary condition at the solid region (eq. 18 and 19) with the non-dimensional length scales of liquid infusion regions, $\frac{\delta_y}{L_y}$ and $\frac{\delta_x}{L_x}$, respectively. It is seen in Figure 4 that the effective slip length of the transverse-striped surface, $\frac{\bar{b}_T^0}{L_x}$, increases with increase in $\frac{\delta_x}{L_x}$ and, similarly, the effective slip length of the longitudinal-striped surface, $\frac{\bar{b}_L^0}{L_y}$, increases with increase in $\frac{\delta_y}{L_y}$. In both cases, as $\frac{\delta_x}{L_x}$ or $\frac{\delta_y}{L_y}$ increases, the amount of solid (no-slip) region in contact with the flowing fluid decreases, leading to an increase in the effective slip length. Further, as the slip length of the infused fluid, b_f, increases (equivalently, as

$\frac{L}{b_f}$ decreases), the fluid flow experiences reduced shear at the surface, leading to an increase in the

effective slip length, for both transverse- $\left(\frac{\overline{b}_T^0}{L_x}\right)$ and longitudinal-striped $\left(\frac{\overline{b}_L^0}{L_y}\right)$ geometries, as evident

in Figure 4. With $b_f \to \infty$ (free shear), both the effective slip length expressions approach the

theoretical formulations derived by Philip[20]. Figure 4 further establishes that the longitudinal-

striped patterning results in a greater slip than the transverse-striped pattern, for a given solid

area fraction $\frac{\delta_x}{L_x}$ or $\frac{\delta_y}{L_y}$, consistent with the results reported in the literature.[20,25]

Figure 5 shows the variation of non-dimensional effective slip length $\frac{\overline{b}}{L}$ for an IHePS

$(L_x = L_y = L)$ surface with the non-dimensional length scale of infusion liquid region in the flow

direction, $\frac{\delta_x}{L}$, for different values of the non-dimensional length scale of infusion liquid region in

the direction perpendicular to the flow, $\frac{\delta_y}{L}$. Figures 5a and 5b present the effect of the slip length

of the infused fluid through the ratio $\frac{L}{b_f}$, for values of 0 and 10, which represents a relevant range

based on typical values of experimentally measured slip length on infusion liquid (b_f) from

$5 - 500\ \mu m$[35]. In each plot, the cases represented by $\frac{\delta_x}{L} \to 0$ and $\frac{\delta_y}{L} \to 0$ correspond to longitudinal

and transverse striped geometries, respectively as discussed earlier. Figure 5 indicates that with

increase in dimensionless length scales of liquid infusion regions, $\frac{\delta_x}{L}$ and $\frac{\delta_y}{L}$, the amount of solid

(no-slip) region in contact with the flowing fluid decreases, leading to an increase in the effective

slip length for all values of $\frac{L}{b_f}$. Further, for any particular combination of $\frac{\delta_x}{L}$ and $\frac{\delta_y}{L}$ values, a direct

comparison between Figures 5a and 5c shows that with increase in the value of the infused fluid

slip length b_f (equivalently, as $\frac{L}{b_f}$ decreases), the effective non-dimensional slip length of the

patterned liquid-infused surface increases. In the limit of $b_f \to \infty$ or $\frac{L}{b_f} \to 0$, which represents a free

shear over the liquid infused regions, the effective slip length approaches the theoretical

formulation derived by Philip[20].

An effect of non-zero slip of fluid flow on liquid-infused structured non-wetting surfaces is

to reduce drag on the surfaces. From eqs. 23 and 25, it is clear that drag reduction under laminar

flow conditions is independent of fluid properties and Reynolds number, but is a function of the

corresponding characteristic flow length scales (H and R), and the effective slip length, $\overline{b}$. Eqs. 23

and 25 suggest that with decrease in the characteristic flow length scales (H and R) (equivalently, with increase in $\frac{L}{H}$ or $\frac{L}{R}$) the percentage drag reduction increases. This is attributed to the increase in flow resistance as a result of increase in solid area fraction per unit volume. For practical purposes, $\frac{L}{H}$ typically takes values in the range 0.01–0.1, and typical infusion liquids have $\frac{L}{b_f}$ values in the range 0–1. Considering selected typical values encountered in practice, the effect of the patterned structure parameters, $\frac{\delta_x}{L}$ and $\frac{\delta_y}{L}$, and infused liquid slip length, $\frac{L}{b_f}$, on the drag reduction for flows in a rectangular channel and a round tube is examined in Figures 6a and 6b, respectively. Figure 6a shows the variation of percentage drag reduction with the dimensionless length scale of infusion liquid along the direction of flow, $\frac{\delta_x}{L}$, for fluid flow between two parallel plates $\left(\frac{L}{H} = 0.01\right)$ made of IHePS superhydrophobic surfaces $\left(\frac{L}{b_f} \to 0\right)$ while Figure 6b presents the variation in a round tube $\left(\frac{L}{R} = 0.1\right)$ with a liquid infused $\left(\frac{L}{b_f} = 1\right)$ IHePS surface. In each plot, the different lines correspond to variation of $\frac{\delta_y}{L}$ in the range 0–1. In addition, the curves corresponding to $\frac{\delta_x}{L} = \frac{\delta_y}{L}$, denoted by the black dashed lines, quantify the percentage drag reduction for the two flow geometries with IHoPS surfaces.

Figures 6a and 6b show that the percentage drag reduction increases with increase in length scale values of liquid-infusion region, $\frac{\delta_x}{L}$ and $\frac{\delta_y}{L}$. For both fluid flow geometries, increase in $\frac{\delta_x}{L}$ and $\frac{\delta_y}{L}$ reduces the solid area fraction (no slip) in contact with the fluid flow, thereby increasing the effective slip length $\overline{b}$ which, in turn, leads to a higher drag reduction. Also, a decrease in the slip length over the infused liquid region, b_f, (equivalently an increase in $\frac{L}{b_f}$) leads to a decrease in the drag reduction, as seen from Figures 6a and 6b. With decreasing b_f values, the flowing fluid experiences increased drag on the infused-liquid region thereby effectively contributing to a smaller drag reduction. Therefore, in general, liquid-infused structured surfaces $\left(\frac{L}{b_f} > 0\right)$ offer less drag reduction compared to structured superhydrophobic surfaces $\left(\frac{L}{b_f} \to 0\right)$.

Figures 7a shows the variation of non-dimensional effective slip length, $\frac{\overline{b}}{L}$, for an IHoPS $\left(\frac{\delta_x}{L} = \frac{\delta_y}{L} = \frac{\delta}{L} = 1 - \sqrt{\varphi_s}\right)$ surface with the solid area fraction in contact with the flowing fluid for

superhydrophobic surfaces, with $\frac{L}{b_f}\to 0$. It is evident from Figure 7a that with increase in the solid area fraction, the effective slip length decreases for all values of $\frac{L}{b_f}$. An increase in the solid area fraction in contact with the flowing fluid increases the no-slip $(b_s = 0)$ region, thereby leading to decrease in the effective slip length, $\bar{b}$. In addition, Figure 7a shows the comparison of the analytical model for the effective slip length on an IHoPS surfaces with several theoretical studies in the literature, for $\frac{L}{b_f}\to 0$ (superhydrophobic surfaces). The current model, as seen in Figure 7a, agrees well with the scaling analysis developed by Ybert *et al.*[27] for solid area fraction, φ_s, greater than about 0.3, and with the asymptotic analytical model developed by Davis and Lauga[26] for circular post geometry patterned in a square array, for solid area fraction, φ_s, greater than about 0.4. In both models[26,27], the dimensionless slip length scales as $1/\sqrt{\varphi_s}$ in the region of small solid area fraction, whereas the present model is based on a detailed physics of the problem over the entire range of solid area fraction. Therefore, the comparison in Figure 7a suggests that the results of the scaling and asymptotic analysis may overpredict the slip length in the range of small solid area fraction values. Further, the analytical solutions in refs. [26] and [27] are for specific *isotropic* geometries, and that too for $b_f\to\infty$ only, whereas, the model presented here is applicable in a generalized manner to isotropic as well as anisotropic and heterogeneous as well as homogeneous topographies, and broadly for any slip length, b_f. To demonstrate the generalized applicability of the model, the data on transverse stripes from Philip[20] is also included in Figure 7a, where it is seen that the current model matches the data closely over the entire range of high solid area fraction ($\varphi_s > \sim 0.6$) reported in their study.

Further, the model is compared with the analytical Wiener and Hashin-Shtrikman bounds on the effective slip length developed for thin channels $(H \ll L)$[22,23] as presented in Figures 7a and 7b. Figure 7a considers the comparison for a superhydrophobic surface $(\frac{L}{b_f}\to 0)$, while Figure 7b presents the comparison for a liquid infused surface with $\frac{L}{b_f} = 10$, both for a nondimensional thin channel thickness of $\frac{H}{L} = 0.01$. Note that the Wiener and Hashin-Shtrikman upper bounds for fluid flow over a superhydrophobic surface approach infinity[22,23] over the entire range of solid area fraction, and are not visible in the plot frame of Figure 7a. Overall, it is seen that the present model

falls within the Wiener and the Hashin-Shtrikman bounds over the entire range of the solid area fraction for both superhydrophobic and liquid infused surfaces, suggesting a broad applicability of the model extending down to thin channels as well.

As mentioned previously, the analytical upper and lower bounds[22,23] are truly valid in the limit of thin channels, $\frac{H}{L} \rightarrow 0$. It is, therefore, of interest to determine an upper limit on H/L for the validity of the analytical bounds. To this end, Figure 7c examines the effect of the nondimensional channel thickness, H/L, on the variation of the upper and the lower bounds on $\overline{b}/L$, for a specific case of $\varphi_s = 0.1$ and $\frac{L}{b_f} = 10$. It is seen that both the Wiener and the Hashin-Shtrikman lower bounds increase with increasing H/L, eventually merging with their respective upper bound. Figure 7c further includes the present model, shown by the red solid line, which falls within the upper and lower bounds for small channel thickness values. At a certain thin nondimensional channel thickness, $\frac{H}{L} = \left(\frac{H}{L}\right)^*$ the dimensionless effective slip length given by each lower bound equals the value given by the present model. The corresponding values of $\left(\frac{H}{L}\right)^*$ indicated in Figure 7c (0.075 and 0.15 for the Hashin-Shtrikman and the Wiener bounds, respectively), may be regarded as the upper limit of the nondimensional thin channel thickness for validity of the Wiener or the Hashin-Shtrikman bound[22,23]

Figure 7c corresponds to a specific case of $\varphi_s = 0.1$ and $\frac{L}{b_f} = 10$; however, in general, the limiting $\left(\frac{H}{L}\right)^*$ values are a function of both the solid area fraction, φ_s, and the slip length of the infused fluid, L/b_f. Figure 7d presents the variation of $\left(\frac{H}{L}\right)^*$ with the solid fraction, for three different values of L/b_f, such that H/L values below each line denote the range of applicability of the analytical bounds based on the thin channel approximation. It is seen that in the limit of $\varphi_s \rightarrow 0$ or $\varphi_s \rightarrow 1$, $\left(\frac{H}{L}\right)^* \rightarrow 0$, but for most of the solid fraction values other than the extreme, the upper limit on the dimensionless channel thickness for each bound varies within a narrow range, for a given L/b_f. As expected from Figure 7c, the upper limit for the Wiener bound is greater than that for the Hashin-Shtrikman bound; in both cases, the upper limit decreases with increasing L/b_f. Overall, it is seen that the bounds[22,23] based on a thin channel assumption are limited to a

maximum nondimensional channel thickness of about 0.3 in the case of the Wiener bound for a superhydrophobic surface and to about 0.15 in the case of the Hashin-Shtrikman bound for the same surface. In contrast, the present model does not have such restriction and is more generally valid for any H/L ratio.

The drag reduction analysis in Figure 6 provides a relative comparison between the structured non-wetting and unstructured smooth surfaces. In order to obtain an intrinsic characteristic of friction on structured non-wetting surfaces, quantification of friction coefficient is conducted using eqs. 24 and 26. Unlike drag reduction, friction coefficient has a dependence on the flow Reynolds number in addition to the structural parameters of the non-wetting surface and the partial slip length, b_f, offered by the infusion liquid. In addition, Eq. 24 and 26 suggest that with decrease in the characteristic flow length scales, H or R (equivalently, as $\frac{L}{H}$ or $\frac{L}{R}$ increases), the friction coefficient decreases. Daniello et $al.$[3] established experimentally that the critical Reynolds number for the transition of fluid flow from laminar to turbulent in microchannels with structured superhydrophobic walls is 2500. Accordingly, the results discussed here are limited to Reynolds number of 2500.

Figure 8 shows the variation of friction coefficient with Reynolds number in the laminar range for different solid area fraction values for IHoPS surfaces ($\delta_x = \delta_y = \delta; L_x = L_y = L$). The selection of solid area fraction values is based on the structural design of non-wetting surfaces. Correspondingly, in Figure 8, solid area fraction values equal to 0, 0.01, 0.1 and 1 represent the cases of purely liquid-infused, typical nano-structured, typical micro-structured and smooth non-structured surfaces, respectively. Figures 8a and 8b show the variation of the friction coefficient on non-wetting surfaces with Reynolds number for fluid flow in the laminar range between bounded plates $\left(\frac{L}{H} = 0.1\right)$ with superhydrophobic $\left(\frac{L}{b_f} \rightarrow 0\right)$ (Figure 8a) and in a round tube with $\frac{L}{R}$ = 0.1 consisting of a liquid-infused IHoPS surface with $\frac{L}{b_f} = 1$ (Figure 8b). Note that the linear variation on the log-log plots in Figures 8a,b, reflect the inverse linear relationship between the friction factor and the Reynolds number ($C_{f,H} = \frac{12}{Re_H}$; $C_{f,R} = \frac{16}{Re_D}$).

For a particular Reynolds number, an increase in the solid area fraction increases the friction coefficient values. Increase in solid area fraction reduces the region of partial slip length leading

to lower effective slip length and thereby higher friction at the interface. The black line in Figures 8a,b, corresponding to $\varphi_s = 1$, represents the case of laminar flow over smooth non-structured surfaces as in the conventional Moody diagram[36]. It is evident from Figures 8a,b that the lines for the structured non-wetting surfaces uniformly fall below the line corresponding to the Moody diagram ($\varphi_s = 1$) pointing to the reduced friction advantage of the non-wetting surfaces. Among the non-wetting surfaces ($\varphi_s < 1$), the presence of infusion liquid with partial slip length (Figure 8b) increases the friction coefficient relative to a superhydrophobic surface (Figure 8a). With a non-zero partial slip at the infused liquid region reduces the effective slip length thereby leading to higher friction at the interface. Figure 8 shows that for all Reynolds numbers, nanostructured surfaces ($\varphi_s \approx 0.01$) offer lower friction coefficient values compared to micro-structured ($\varphi_s \approx 0.1$) and smooth non-structured ($\varphi_s = 1$) surfaces.

Figures 9a and 9b show the variation of percentage drag reduction with solid area fraction for a fluid flow in a round tube with superhydrophobic $\left(\frac{L}{b_f} \to 0\right)$ and a parallel channel with liquid infused $\left(\frac{L}{b_f} = 1\right)$ surfaces, respectively, for a range of flow characteristic length scale values $\frac{L}{R}$ and $\frac{L}{H}$. Corresponding to each value of $\frac{L}{R}$ and $\frac{L}{H}$, three distinct curves representing longitudinal-striped, transverse-striped and IHoPS surfaces are presented. From Figures 9a and 9b it is evident that for a particular value of $\frac{L}{R}$ or $\frac{L}{H}$, nanostructured surfaces ($\varphi_s \lesssim 0.08$) offer significantly higher drag reduction compared to micro-structured ($0.08 \lesssim \varphi_s \lesssim 0.2$) surfaces. Also, for a particular non-wetting surface, decreasing the flow characteristic length scale, R or H (equivalently, increasing $\frac{L}{R}$ or $\frac{L}{H}$) increases the percentage drag reduction, as seen from Figures 9a and 9b. Liquid-infused surfaces $\left(\frac{L}{b_f} = 1\right)$ are seen to offer lower drag reduction (Figure 9b) compared to superhydrophobic surfaces $\left(\frac{L}{b_f} \to 0\right)$ (Figure 9a), owing to the finite partial slip length (b_f) in the infused liquid region. The observed trends are common to both channel flows as well as flows in cylindrical tubes.

Figures 9c and 9d show contours of constant percentage drag reduction as the dimensionless flow characteristic length scale $\frac{L}{R}$ or $\frac{L}{H}$ and the solid area fraction are varied, corresponding to the

respective flow configurations in Figures 9a and 9b, respectively. These figures serve as example design plots for the design of the structural parameters of the patterned surfaces, for achieving target drag reduction values. For a particular desired percentage drag reduction, nanostructured surfaces ($\varphi_s \lesssim 0.08$) allow for bigger flow length scales (larger H, equivalently smaller $\frac{L}{H}$, or larger radius, R, equivalently, smaller $\frac{L}{R}$). Figures 9c and 9d also show that the use of liquid infused surfaces $\left(\frac{L}{b_f} = 1\right)$ limits the maximum flow length scales (smaller H, equivalently larger $\frac{L}{H}$, or smaller radius, R, equivalently, larger $\frac{L}{R}$) for achieving the same percentage drag reduction as with superhydrophobic surfaces $\left(\frac{L}{b_f} \to 0\right)$.

The present formulations for drag reduction takes into consideration the effects of various characteristic parameters, such as, surface heterogeneity, structural anisotropy, and partial slip offered by infusion liquid. In order to validate the current model, results from a number of experimental and computational studies are borrowed from the literature, and a comparison of the model predictions relative to the literature data is presented in Figure 10. The selection of literature studies for comparison was prioritized with the focus on covering a variety of surface topologies and fluid flow conditions, and a wide range of nondimensional channel thickness. As a result, superhydrophobic surfaces with surface topologies namely, microridges [37], square posts [30], circular posts [38], grates [38] and carbon nanotube forest [39] are considered for the comparison. From Ou and Rothstein[37], two different microridge geometries are considered: the experimental and numerical simulation results for 20 µm wide microridges spaced $\delta_y = 20$ µm apart are denoted by the red circular markers and the red solid line, respectively and the experimental and numerical simulation results corresponding to 30 µm wide microridges spaced $\delta_y = 30$ µm apart are represented by the blue square markers and the blue solid line, respectively. The experimental study by Ou et al.[30] on microchannel flows with square post surface topography is presented by the green diamond markers. Lee et al.[38] presented data from a rheometer test wherein the solid area fraction was varied by manipulating the pitch of homogeneously patterned circular posts (shown by inverted triangle markers in Fig. 10). Joseph et al.[39] considered the case of carbon nanotube forest offering a solid area fration of $\varphi_s = 0.1$ (right triangle markers) and the

experimental results of Solomon *et al.*[28] (purple triangle markers) correspond to the drag reduction offered by liquid infused non-wetting surfaces with $\frac{L}{b_f} = 2.77$. Owing to the considerable drag reduction for microscale values of flow length scales, the majority of the studies have considered fluid flow in microchannels and cone-plate rheometer assembly with separation of the order of $O(10^2)$ micrometers. The data considered for comparison cover a wide range of nondimensional channel thickness H/L range from 2 to 333, which complement the thin channel thickness range discussed in Figure 7.

The solid line diagonal to the plot frame in Figure 10 represents the line of exact agreement, while the dashed lines on either side of the solid line denote the $\pm 5\%$ error bands. The drag reduction being a percentage itself, the error bands are shown as absolute error bands. From Figure 10, it is evident that the present model compares well, to within $\pm 5\%$, with nearly all the cases. The data of Ou and Rothstein[37] on the 30 μm wide microridges spaced $\delta_y = 30$ μm apart (red circular markers) are seen to lie at or above the $+5\%$ error band and represent the most disparity with respect to the present model. However, their data also lie above their own model (red line), which itself falls within $+5\%$ of the present model predictions. Moreover, the experimental data as well as the model predictions of Ou and Rothstein[37] for 20 μm wide microridges spaced $\delta_y = 20$ μm apart are seen to agree with the current model predictions well. Further, the model is seen to closely match the experimental results of Solomon *et al.*,[28] Lee *et al.*,[38] and Joseph *et al.*[39] It is also evident from the comparison in Figure 10 that the present model predictions tend to be conservative in estimating the drag reduction, and that the actual drag reduction could be greater by up to 5% in practice. The model may, therefore, be useful in practical design exercise with an inherent safety margin. The present model is seen to be generally valid for any H/L ratio, where it falls within the Wiener and Hashin-Shrikman bounds[22-23] for thin channels in Figures 7a-7c, and as shown in Figure 10, also compares well with data from a variety of literature sources for thick channels with $H/L = 2$–333.

The results presented in this study provide analytical formulations for effective slip length, drag reduction and friction coefficient calculations for laminar flow over anisotropic heterogeneously patterned structured surfaces. Overall, the results demonstrate the generalized applicability of the present model to a wide range of topographies, infused liquid parameters,

and channel thickness, which forms the primary contribution of the article. The analytical solutions can be used for designing a variety of fluid and thermal systems such as heat exchangers by tailoring surface patterns for achieving desired drag reduction and friction coefficient. It was seen that the liquid infused structured surfaces provide less drag reduction compared to superhydrophobic surfaces with air cavities under Cassie state. However, it is well-known that superhydrophobic surfaces degrade from the Cassie state of wettability to the Wenzel state, which might limit the durability of the drag reduction advantage over liquid-infused patterned surfaces, as considered in a separate study[40]. Furthermore, liquid-infused surfaces are expected to provide enhanced heat transfer rate compared to superhydrophobic surfaces, that would be relevant for a number of applications such as pool/flow boiling, drop-wise condensation, etc. While the focus of the present study was on the fluid flow aspects, heat transfer characteristics of structured non-wetting surfaces will be considered in a future work. Similarly, extension of the study to non-Newtonian and turbulent flows will also be addressed in a future study.

5. CONCLUSIONS

An analytical model was developed for prediction of finite effective slip and, in turn, drag reduction and friction coefficient on liquid-infused structured non-wetting surfaces. The analytical solution is purely in terms of the geometrical parameters of the patterned surface and the infusing fluid, and eliminates empirical fitting or correlations that are inherent in previous studies. Based on the slip length and drag reduction values, it is shown that superhydrophobic surfaces are significantly better in their non-wetting characteristics compared to liquid-infused structured surfaces. Also, the laminar flow conditions considered in the present study limit the drag reduction to about 40% for a practical range of fluid flow characteristic length-scales, as seen in Figures 9 and 10. Design plots are presented to determine the choice of meso-, micro- or nano structured non-wetting surface geometrical parameters (φ_s and L) for a given channel/tube dimension, so as to achieve a desired drag reduction. The theoretical solutions from the present study closely agree with experimental and computational data on effective slip and drag reduction reported in the literature for a wide range of governing parameters.

6. ACKNOWLEDGMENT AND DISCLAIMER

NOMENCLATURE

b_s: Fluid flow slip length on solid region

b_f: Fluid flow slip length on infusion liquid region

δ_x: Liquid infusion region length scale in the direction of flow

δ_y: Solid region length scale in the direction perpendicular to the flow

L_x: Periodic length scale of posts in the direction of flow

L_y: Periodic length scale of posts in the direction perpendicular to the flow

H: Separation between two infinite parallel plates

R: Radius of a round tube (cylindrical geometry)

u: Velocity component in the direction of flow

η: Dynamic viscosity

p: Pressure

σ_0:   Pressure gradient in the direction of flow

u_0:   Base flow velocity

25

u':   Perturbation velocity

ψ: Stream function

ψ_0:   Base flow stream function

ψ':   Perturbation stream function

ω: Vorticity

ω_0:   Base flow vorticity

ω':   perturbation vorticity

b_L: Effective slip length on longitudinal striped geometry

b_T: Effective slip length on transverse striped geometry

b_L^0:   Effective slip length on longitudinal striped geometry with zero slip on solid region

b_T^0:   Effective slip length on transverse striped geometry with zero slip on solid region

$\overline{b}$:   Effective slip length on structured non-wetting surfaces

φ_s: Solid area fraction

Q: Volume flow rate

D_R: Drag reduction

C_f: Coefficient of friction

τ_s: Shear stress

ρ: Fluid density

Re: Reynolds number

Subscripts

0:        Smooth surface

s: Structured non-wetting surface

L: Case of longitudinal stripes

T: Case of transverse stripes

H: Case of fluid flow between two infinite parallel plates

R: Case of fluid flow in round tubes (cylindrical geometry)

Acronyms

SLIPS :   Slippery liquid infused porous surface

SH :   Superhydrophobic

AHePS :   Anisotropic heterogeneously patterned structured

IHePS :   Isotropic heterogeneously patterned structured

IHoPS :   Isotropic homogeneously patterned structured

7. REFERENCES

(1)   Choi, C. H.; Ulmanella, U.; Kim, J.; Ho, C. M.; Kim, C. J. Effective Slip and Friction Reduction in Nanograted Superhydrophobic Microchannels. *Phys. Fluids* **2006**, *18* (8). https://doi.org/10.1063/1.2337669.

(2)   Dong, H.; Cheng, M.; Zhang, Y.; Wei, H.; Shi, F. Extraordinary Drag-Reducing Effect of a Superhydrophobic Coating on a Macroscopic Model Ship at High Speed. *J. Mater. Chem. A* **2013**, *1* (19), 5886–5891. https://doi.org/10.1039/c3ta10225d.

(3)   Daniello, R. J.; Waterhouse, N. E.; Rothstein, J. P. Drag Reduction in Turbulent Flows over Superhydrophobic Surfaces. *Phys. Fluids* **2009**, *21* (8). https://doi.org/10.1063/1.3207885.

(4)   Miljkovic, N.; Enright, R.; Nam, Y.; Lopez, K.; Dou, N.; Sack, J.; Wang, E. N. Jumping-Droplet-Enhanced Condensation on Scalable Superhydrophobic Nanostructured Surfaces. *Nano Lett.* **2013**, *13* (1), 179–187. https://doi.org/10.1021/nl303835d.

(5)   Chen, C. H.; Cai, Q.; Tsai, C.; Chen, C. L.; Xiong, G.; Yu, Y.; Ren, Z. Dropwise Condensation on Superhydrophobic Surfaces with Two-Tier Roughness. *Appl. Phys. Lett.* **2007**, *90* (17), 2005–2008. https://doi.org/10.1063/1.2731434.

(6)   Miljkovic, N.; Preston, D. J.; Enright, R.; Wang, E. N. Electric-Field-Enhanced Condensation on Superhydrophobic Nanostructured Surfaces. *ACS Nano* **2013**, *7* (12), 11043–11054. https://doi.org/10.1021/nn404707j.

(7)   Ramakrishna, S.; Kumar, K. S. S.; Mathew, D.; Reghunadhan Nair, C. P. A Robust, Melting Class Bulk Superhydrophobic Material with Heat-Healing and Self-Cleaning Properties. *Sci. Rep.* **2015**, *5* (December). https://doi.org/10.1038/srep18510.

(8)   Fürstner, R.; Barthlott, W.; Neinhuis, C.; Walzel, P. Wetting and Self-Cleaning Properties of Artificial Superhydrophobic Surfaces. *Langmuir* **2005**, *21* (3), 956–961. https://doi.org/10.1021/la0401011.

(9)   Park, Y. B.; Im, H.; Im, M.; Choi, Y. K. Self-Cleaning Effect of Highly Water-Repellent Microshell Structures for Solar Cell Applications. *J. Mater. Chem.* **2011**, *21* (3), 633–636. https://doi.org/10.1039/c0jm02463e.

(10)   Wang, Y.; Xue, J.; Wang, Q.; Chen, Q.; Ding, J. Verification of Icephobic/Anti-Icing Properties of a Superhydrophobic Surface. *ACS Appl. Mater. Interfaces* **2013**, *5* (8), 3370–

3381. https://doi.org/10.1021/am400429q.

(11)   Ruan, M.; Li, W.; Wang, B.; Deng, B.; Ma, F.; Yu, Z. Preparation and Anti-Icing Behavior of Superhydrophobic Surfaces on Aluminum Alloy Substrates. *Langmuir* **2013**, *29* (27), 8482–8491. https://doi.org/10.1021/la400979d.

(12)   Boreyko, J. B.; Collier, C. P. Delayed Frost Growth on Jumping-Drop Superhydrophobic Surfaces. *ACS Nano* **2013**, *7* (2), 1618–1627. https://doi.org/10.1021/nn3055048.

(13)   Wong, T. S.; Kang, S. H.; Tang, S. K. Y.; Smythe, E. J.; Hatton, B. D.; Grinthal, A.; Aizenberg, J. Bioinspired Self-Repairing Slippery Surfaces with Pressure-Stable Omniphobicity. *Nature* **2011**, *477* (7365), 443–447. https://doi.org/10.1038/nature10447.

(14)   Lafuma, A.; Quéré, D. Slippery Pre-Suffused Surfaces. *Epl* **2011**, *96* (5). https://doi.org/10.1209/0295-5075/96/56001.

(15)   Bhushan, B.; Jung, Y. C. Natural and Biomimetic Artificial Surfaces for Superhydrophobicity, Self-Cleaning, Low Adhesion, and Drag Reduction. *Prog. Mater. Sci.* **2011**, *56* (1), 1–108. https://doi.org/10.1016/j.pmatsci.2010.04.003.

(16)   Cottin-Bizonne, C.; Barrat, J. L.; Bocquet, L.; Charlaix, E. Low-Friction Flows of Liquid at Nanopatterned Interfaces. *Nat. Mater.* **2003**, *2* (4), 237–240. https://doi.org/10.1038/nmat857.

(17)   Vinogradova, O. I. Drainage of a Thin Liquid Film Confined between Hydrophobic Surfaces. *Langmuir* **1995**, *11* (6), 2213–2220. https://doi.org/10.1021/la00006a059.

(18)   Rothstein, J. P. Slip on Superhydrophobic Surfaces. **2010**. https://doi.org/10.1146/annurev-fluid-121108-145558.

(19)   Voronov, R. S.; Papavassiliou, D. V; Lee, L. L. Review of Fluid Slip over Superhydrophobic Surfaces and Its Dependence on the Contact Angle. **2008**, 2455–2477. https://doi.org/10.1021/ie0712941.

(20)   Philip, J. R. Flows Satisfying Mixed No-Slip and No-Shear Conditions. *Zeitschrift für Angew. Math. und Phys. ZAMP* **1972**, *23* (3), 353–372. https://doi.org/10.1007/BF01595477.

(21)   Lauga, E.; Stone H. A. Effective Slip in Pressure-Driven Stokes Flow. **2003**, *489*, 55–77. *J. Fluid Mech.* https://doi.org/10.1017/S0022112003004695.

(22)   Feuillebois, F.; Bazant, M. Z.; Vinogradova, O. I. Effective Slip over Superhydrophobic Surfaces in Thin Channels. **2009**. https://doi.org/10.1103/PhysRevLett.102.026001.

(23)   Feuillebois, F.; Bazant, M. Z.; Vinogradova, O. I. Erratum : Effective Slip over Superhydrophobic Surfaces in Thin Channels. **2010**, *159902* (April), 159902. https://doi.org/10.1103/PhysRevLett.104.159902.

(24)   Feuillebois, F.; Bazant, M. Z.; Vinogradova, O. I. Transverse Flow in Thin Superhydrophobic Channels 1. **2010**, 1–4. https://doi.org/10.1103/PhysRevE.82.055301.

(25)   Belyaev, A. V.; Vinogradova, O. I. Effective Slip in Pressure-Driven Flow Past Super-Hydrophobic Stripes. *J. Fluid Mech.* **2010**, *652*, 489–499. https://doi.org/10.1017/S0022112010000741.

(26)   Davis, A. M. J.; Lauga, E. Hydrodynamic Friction of Fakir-like Superhydrophobic Surfaces. *J. Fluid Mech.* **2010**, *661*, 402–411. https://doi.org/10.1017/S0022112010003460.

(27)   Ybert, C.; Barentin, C.; Cottin-Bizonne, C.; Joseph, P.; Bocquet, L. Achieving Large Slip with Superhydrophobic Surfaces: Scaling Laws for Generic Geometries. *Phys. Fluids* **2007**, *19* (12). https://doi.org/10.1063/1.2815730.

(28)   Solomon, B. R.; Khalil, K. S.; Varanasi, K. K. Drag Reduction Using Lubricant-Impregnated Surfaces in Viscous Laminar Flow. *Langmuir* **2014**, *30* (36), 10970–10976. https://doi.org/10.1021/la5021143.

(29)   Cottin-Bizonne, C.; Barentin, C.; Bocquet, L. Scaling Laws for Slippage on Superhydrophobic Fractal Surfaces. *Phys. Fluids* **2012**, *24* (1). https://doi.org/10.1063/1.3674300.

(30)   Ou, J.; Perot, B.; Rothstein, J. P. Laminar Drag Reduction in Microchannels Using Ultrahydrophobic Surfaces. *Phys. Fluids* **2004**, *16* (12), 4635–4643. https://doi.org/10.1063/1.1812011.

(31)   Gogte, S.; Vorobieff, P.; Truesdell, R.; Mammoli, A.; Van Swol, F.; Shah, P.; Brinker, C. J. Effective Slip on Textured Superhydrophobic Surfaces. *Phys. Fluids* **2005**, *17* (5), 1–4. https://doi.org/10.1063/1.1896405.

(32)   Srinivasan, S.; Choi, W.; Park, K. C.; Chhatre, S. S.; Cohen, R. E.; McKinley, G. H. Drag Reduction for Viscous Laminar Flow on Spray-Coated Non-Wetting Surfaces. *Soft Matter* **2013**, *9* (24), 5691–5702. https://doi.org/10.1039/c3sm50445j.

(33)   I. N. Sneddon. Mixed Boundary Value Problems in Potential Theory. *North-holl. Publ. Co.*

1966, 2020.

(34)　Priezjev, N. V.; Darhuber, A. A.; Troian, S. M. Slip Behavior in Liquid Films on Surfaces of Patterned Wettability: Comparison between Continuum and Molecular Dynamics Simulations. *Phys. Rev. E - Stat. Nonlinear, Soft Matter Phys.* **2005**, *71* (4), 1–11. https://doi.org/10.1103/PhysRevE.71.041608.

(35)　Quéré, D. Non-Sticking Drops. *Reports Prog. Phys.* **2005**, *68* (11), 2495–2532. https://doi.org/10.1088/0034-4885/68/11/R01.

(36)　Merci, B. *Introduction to Fluid Mechanics*; John Wiley & Sons, 2016. https://doi.org/10.1007/978-1-4939-2565-0_1.

(37)　Ou, J.; Rothstein, J. P. Direct Velocity Measurements of the Flow Past Drag-Reducing Ultrahydrophobic Surfaces. *Phys. Fluids* **2005**, *17* (10). https://doi.org/10.1063/1.2109867.

(38)　Lee, C.; Choi, C. H.; Kim, C. J. Structured Surfaces for a Giant Liquid Slip. *Phys. Rev. Lett.* **2008**, *101* (6), 1–4. https://doi.org/10.1103/PhysRevLett.101.064501.

(39)　Joseph, P.; Cottin-Bizonne, C.; Benoît, J. M.; Ybert, C.; Journet, C.; Tabeling, P.; Bocquet, L. Slippage of Water Past Superhydrophobic Carbon Nanotube Forests in Microchannels. *Phys. Rev. Lett.* **2006**, *97* (15), 1–4. https://doi.org/10.1103/PhysRevLett.97.156104.

(40)　Hatte, S.; Pitchumani, R. Fractal Model for Drag Reduction on Multiscale Non-wetting Rough Surfaces, *Langmuir*, **2021**, https://dx.doi.org/10.1021/acs.langmuir.0c02790.

Table 1. List of governing equations and associated boundary conditions for total velocity and perturbation velocity, for flow over a longitudinal-striped geometry (Figures 1b-c).

	Total velocity, $u(y,z)$		Perturbation velocity, $u'(y,z)$	
Governing equations	$\dfrac{\partial^2 u}{\partial y^2} + \dfrac{\partial^2 u}{\partial z^2} = \dfrac{1}{\eta}\dfrac{dp}{dx}$	(1a)	$\dfrac{\partial^2 u'}{\partial y^2} + \dfrac{\partial^2 u'}{\partial z^2} = 0$	(3a)
Boundary conditions	$\dfrac{\partial u}{\partial y}(0,z) = 0$	(1b)	$\dfrac{\partial u'}{\partial y}(0,z) = 0$	(3b)
	$u(y,z) = u(y + L_y,z)$	(1c)	$u'(y,z) = u'(y + L_y,z)$	(3c)
	$\dfrac{\partial u}{\partial z}\left(y,\dfrac{H}{2}\right) = 0$	(1d)	$\dfrac{\partial u'}{\partial z}\left(y,\dfrac{H}{2}\right) = 0$	(3d)
	$u(y,0) = b(y)\dfrac{\partial u}{\partial z}(y,0)$	(1e)	$u'(y,z=0) = \begin{cases} b_f\dfrac{\partial u'}{\partial z}(y,z=0) - \dfrac{H}{2\eta}\dfrac{dp}{dx}b_f & \left(0 \le y \le \dfrac{\delta_y}{2}\right) \\[2ex] b_s\dfrac{\partial u'}{\partial z}(y,z=0) - \dfrac{H}{2\eta}\dfrac{dp}{dx}b_s & \left(\dfrac{\delta_y}{2} \le y \le \dfrac{L_y}{2}\right) \end{cases}$	(3e)

Table 2. List of governing equations and boundary conditions for stream function, vorticity and perturbation functions of stream function and vorticity, for flow over a transverse-striped geometry (Figures 1d-e).

	Stream function, $\psi(x,z)$, and vorticity, $\omega(x,z)$				Perturbation of stream function, $\psi'(x,z)$, and vorticity, $\omega'(x,z)$			
Governing equations	$\dfrac{\partial^2 \psi}{\partial x^2} + \dfrac{\partial^2 \psi}{\partial z^2} = \omega$	(8a)	$\dfrac{\eta}{\rho}\left(\dfrac{\partial^2 \omega}{\partial x^2} + \dfrac{\partial^2 \omega}{\partial z^2}\right) = \dfrac{\partial \psi}{\partial z}\dfrac{\partial \omega}{\partial x} - \dfrac{\partial \psi}{\partial x}\dfrac{\partial \omega}{\partial z}$	(9a)	$\dfrac{\partial^2 \psi'}{\partial x^2} + \dfrac{\partial^2 \psi'}{\partial z^2} = \omega'$	(12a)	$\dfrac{\partial^2 \omega'}{\partial x^2} + \dfrac{\partial^2 \omega'}{\partial z^2} = 0$	(13a)
Boundary conditions	$\dfrac{\partial \psi}{\partial x}(x,0) = 0$	(8b)	$\dfrac{\partial \omega}{\partial x}(0,z) = 0$	(9b)	$\dfrac{\partial \psi'}{\partial x}(x,0) = 0$	(12b)	$\dfrac{\partial \omega'}{\partial x}(0,z) = 0$	(13b)
	$\dfrac{\partial \psi}{\partial x}(x,H) = 0$	(8c)	$\dfrac{\partial \omega}{\partial x}\left(\dfrac{L_x}{2},z\right) = 0$	(9c)	$\dfrac{\partial \psi'}{\partial x}(x,H) = 0$	(12c)	$\dfrac{\partial \omega'}{\partial x}\left(\dfrac{L_x}{2},z\right) = 0$	(13c)
	$\dfrac{\partial \psi}{\partial x}(0,z) = 0$	(8d)	$\omega(x,0) = \dfrac{1}{b(x)}\dfrac{\partial \psi}{\partial z}(x,0)$	(9d)	$\dfrac{\partial \psi'}{\partial x}(0,z) = 0$	(12d)	$\omega'(x,0) = \dfrac{1}{b(x)}\dfrac{\partial \psi'}{\partial z}(x,0) - \dfrac{H}{2\eta}\dfrac{dp}{dx}$	(13d)
	$\dfrac{\partial \psi}{\partial x}\left(\dfrac{L_x}{2},z\right) = 0$	(8e)	$\omega(x,H) = -\dfrac{1}{b(x)}\dfrac{\partial \psi}{\partial z}(x,H)$	(9e)	$\dfrac{\partial \psi'}{\partial x}\left(\dfrac{L_x}{2},z\right) = 0$	(12e)	$\omega'(x,H) = -\dfrac{1}{b(x)}\dfrac{\partial \psi'}{\partial z}(x,H) + \dfrac{H}{2\eta}\dfrac{dp}{dx}$	(13e)

FIGURE CAPTIONS

Figure 1.   (a) Isometric view of a typical liquid infused AHePS surface, (b) Isometric and (c) top view of a typical liquid infused longitudinal striped geometry and (d) Isometric and (e) top view of a typical liquid infused transverse striped geometry, with associated geometric parameters.

Figure 2.   Schematic representation of (a) flow in a rectangular channel formed between two parallel liquid infused AHePS surfaces separated by a distance H, and (b) flow in a round tube with inner wall structured with liquid infused AHePS patterns.

Figure 3.   Schematic representation of the methodology to calculate the effective slip length on a liquid infused AHePS surface: (a) rectangular regions marked T constitute transverse stripes (with an effective slip length b_T^0), which together with the infused liquid region form an equivalent longitudinal-striped geometry; (b) regions marked L constitute longitudinal stripes (with an effective slip length b_L^0), which together with the infused liquid region form an equivalent transverse-striped geometry.

Figure 4.   Variation of the effective slip length for longitudinal- and transverse-striped geometries with the AHePS geometric parameters, δ_x/L_x and δ_y/L_y for different dimensionless partial slip length (L/b_f) values of the infused liquid region.

Figure 5.   Variation of the dimensionless effective slip length ($\bar{b}/L$) on liquid infused isotropic heterogeneously patterned structured (IHePS) surface with δ_x/L and δ_y/L, for (a) $\frac{L}{b_f} \to 0$ and (b) $\frac{L}{b_f} = 10$.

Figure 6.   Variation of percentage drag reduction with δ_x/L for fluid flow (a) between two infinite parallel plates with superhydrophobic IHePS $\left(\frac{L}{b_f} \to 0\right)$ and (b) in a round tube with liquid infused $\left(\frac{L}{b_f} = 1\right)$ IHePS walls, for characteristic flow length scale $\frac{L}{H} = \frac{L}{R}$ $= 0.01$ and for a range of δ_y/L values.

Figure 7.   Variation of the dimensionless effective slip length ($\bar{b}/L$) with sold area fraction (φ_s) for (a) superhydrophobic and (b) liquid infused $\left(\frac{L}{b_f} = 10\right)$, isotropic homogeneously patterned surface (IHoPS) for $\frac{H}{L} = 0.01$; (c) variation of the nondimensional effective

slip length with dimensionless channel thickness comparing the present model with analytical upper and lower bounds[22,23]; and (d) variation of the upper limit of dimensional channel thickness with solid fraction establishing the range of validity of the analytical bounds[22,23].

Figure 8. Variation of friction coefficient with Reynolds number for fluid flow (a) between two infinite parallel plates with superhydrophobic IHoPS ($\frac{L}{b_f}\to\infty$) and (b) in a round tube with liquid infused IHoPS wall ($\frac{L}{b_f}=1$) for characteristic flow length scale $\frac{L}{H}=\frac{L}{R}=0.01$, and different solid fraction, φ_s.

Figure 9. Variation of percentage drag reduction with solid area fraction for fluid flow (a) in a round tube with superhydrophobic IHoPS $\left(\frac{L}{b_f}\to0\right)$ and (b) between two infinite parallel plates with liquid infused $\left(\frac{L}{b_f}=1\right)$ surfaces, for a range of flow characteristic length scale values $\frac{L}{R}$ and $\frac{L}{H}$, respectively, and variation of flow characteristic length scales (c) $\frac{L}{R}$ and (d) $\frac{L}{H}$ with solid area fraction for a range of drag reduction values.

Figure 10. Comparison of the percentage drag reduction predicted by the analytical model developed in the present study with experimental data and computational simulation results reported in the literature for different structured geometries: 20 μm wide microridges spaced 20 μm apart (●), 30 μm wide microridges spaced 30 μm apart (■), 30 μm wide square posts spaced 30 μm apart (♦), circular posts (▼),carbon nanotube forest SH structures at solid area fraction 0.1 (◢) , liquid-infused structured surfaces (▲), computational results for 20 μm wide microridges spaced 20 μm apart (▬▬▬), and 30 μm wide micro-ridges spaced 30 μm apart (▬▬▬).
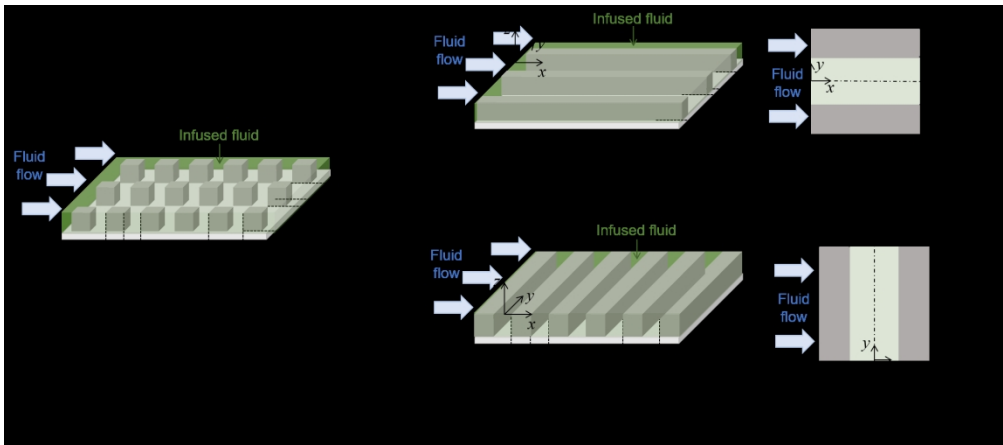
Figure 1

378x167mm (150 x 150 DPI)
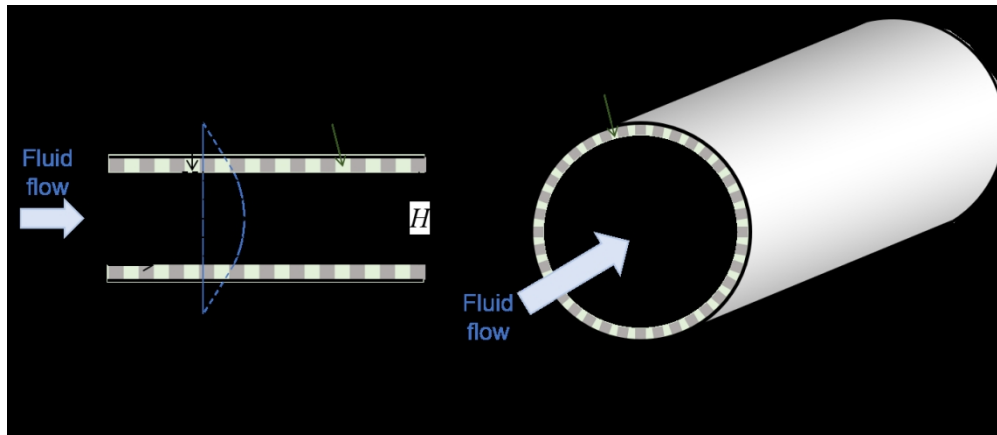
Figure 2

235x101mm (150 x 150 DPI)
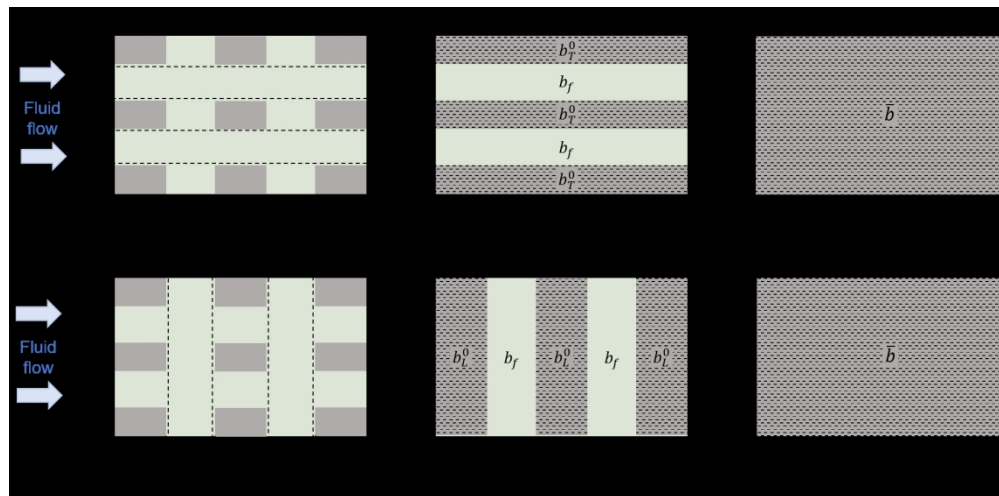
Figure 3

329x162mm (150 x 150 DPI)
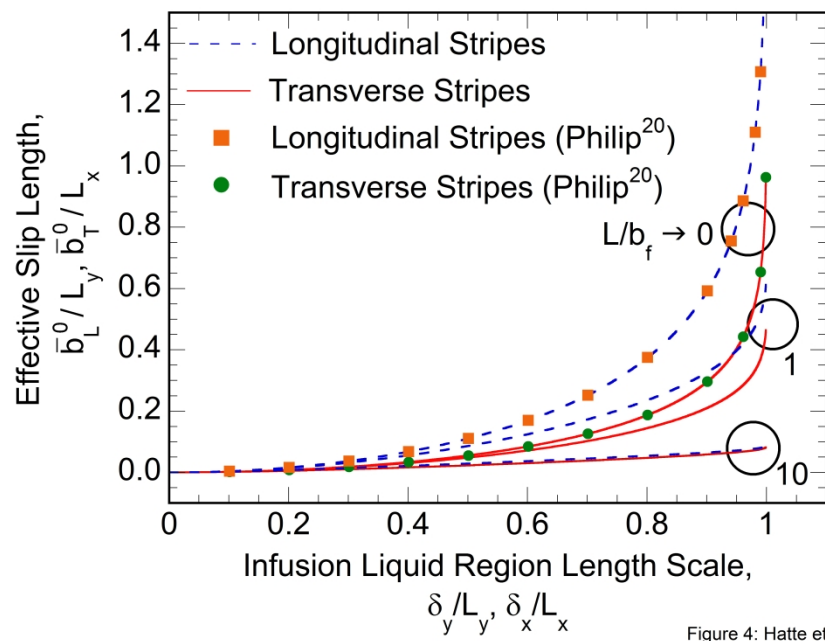
Figure 4: Hatte et al.

Figure 4

270x206mm (576 x 576 DPI)

Figure 5
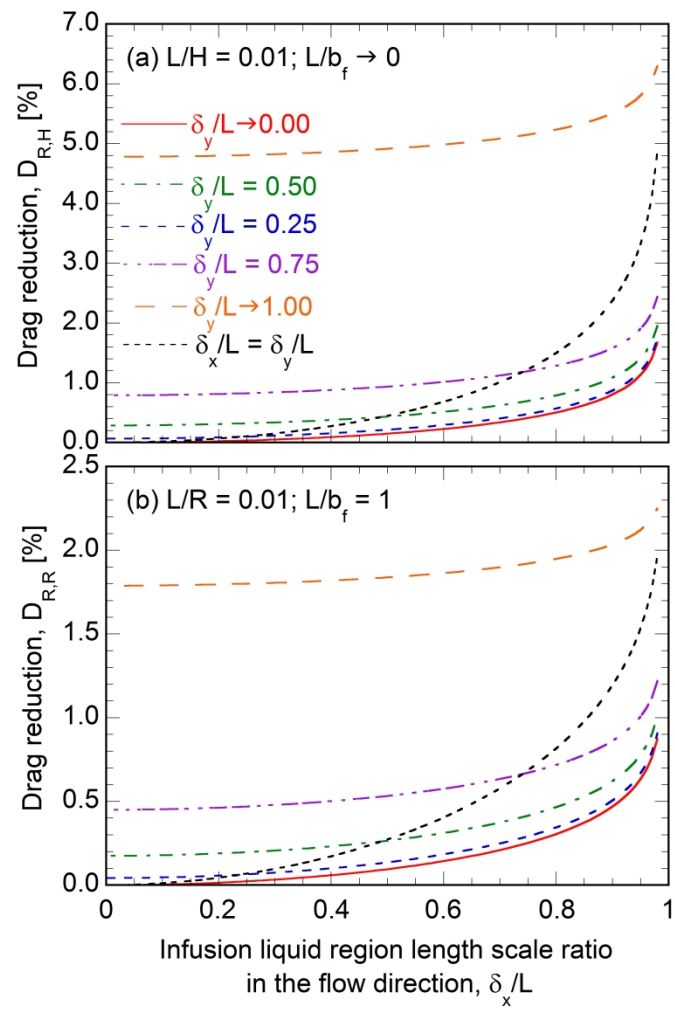
Figure 6: Hatte et al.

Figure 6

207x270mm (576 x 576 DPI)
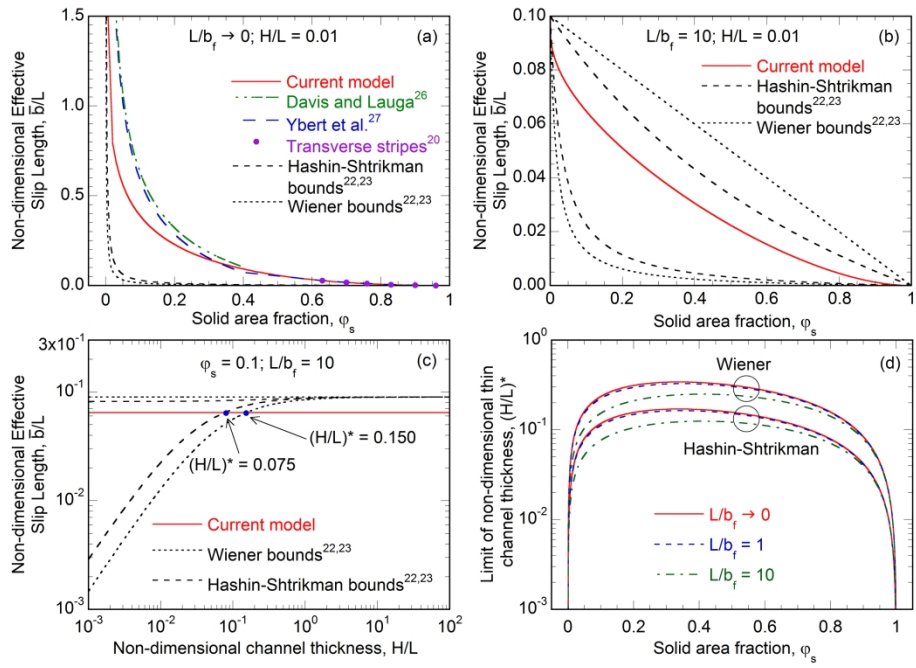
Figure 7

269x207mm (300 x 300 DPI)
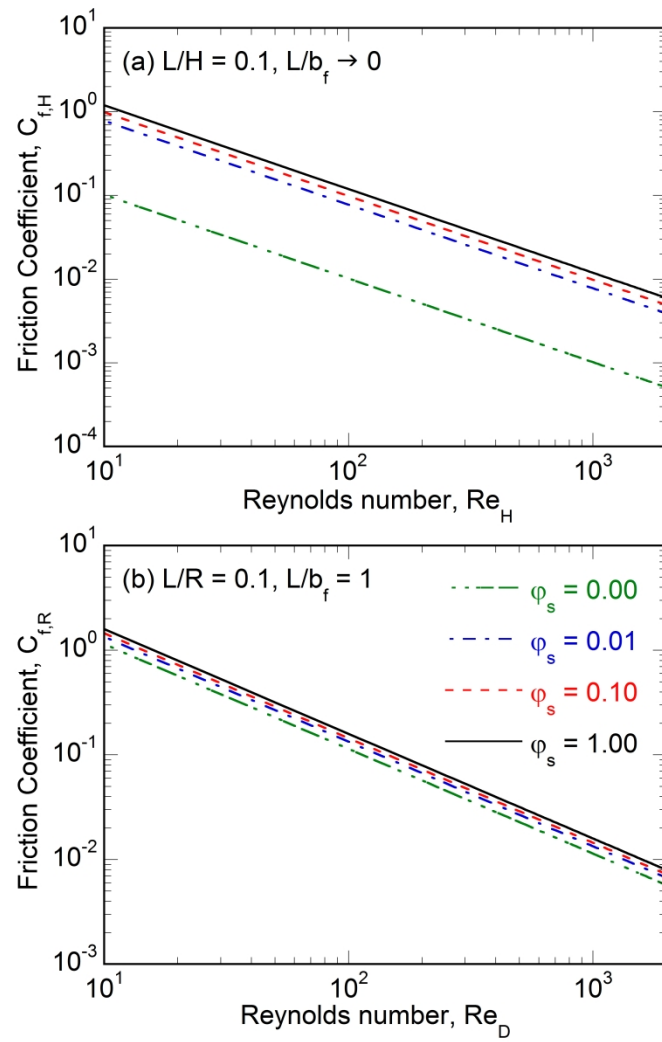
Figure 8: Hatte et al.

Figure 8

207x270mm (576 x 576 DPI)
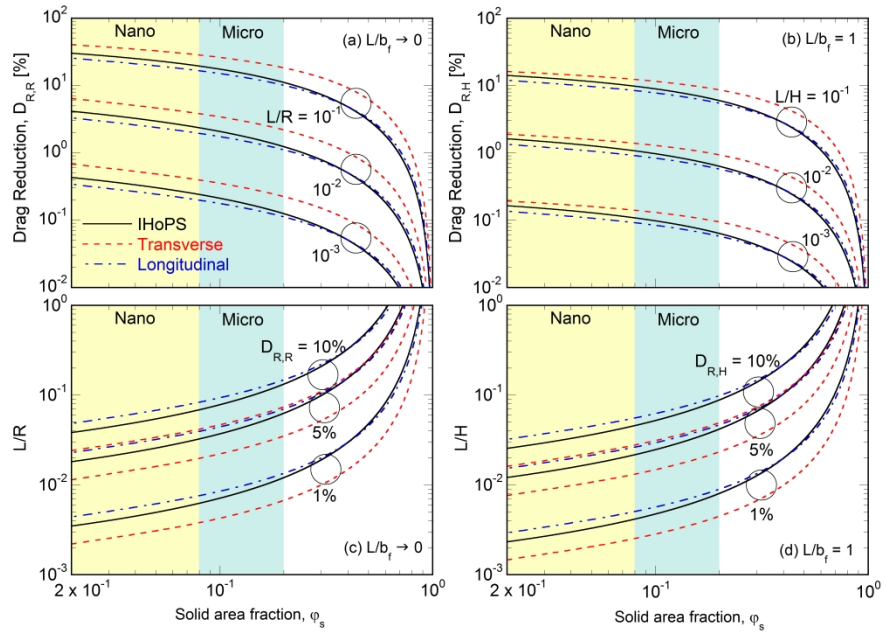
Figure 9: Hatte et al.

Figure 9

269x207mm (576 x 576 DPI)
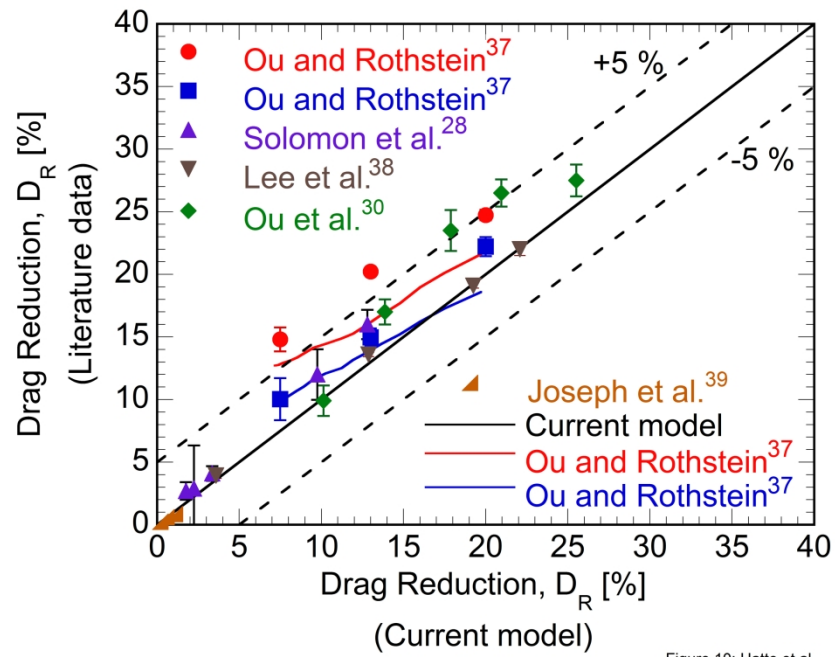
Figure 10: Hatte et al.

Figure 10

270x206mm (300 x 300 DPI)

336x95mm (150 x 150 DPI)